Supporting Information

Solvothermal-assisted defect engineering in hierarchically porous carbonized wood fibers for high-performance lithium-sulfur batteries

*Yangyang Chen, Yu Liao, Lei Li, Yiding Ding, Ying Wu, Zhen Zhang, Sha Luo, Yiqiang Wu and Yan Qing**

College of Materials Science and Technology, Central South University of Forestry and Technology, Changsha 410004, China.

*Corresponding author

E-mail address: qingyan0429@163.com

1. Experimental section

1.1 Materials

All reagents utilized in this study were of analytical grade and employed without additional purification. 2-ethoxyethanol ($C_4H_{10}O_2$, ≥99.8%), and ethylene glycol ($C_2H_6O_2$, ≥99.9%) were bought from Aladdin Biochemical Technology Co., Ltd. Ethyl ether ($C_4H_{10}O$, ≥99.5 %) was bought from Sinopharm Chemical Reagent Co., Ltd. In this study, ultrapure water was employed.

1.2 Synthesis of the Li_2S_6 solution

To prepare Li_2S_6 solution (0.5 M), Sulfur and Li_2S (Sigma-Aldrich) were mixed to Dioxolane (DOL) and Dimethoxyethane (DME) (Sigma Aldrich) (1:1 in volume) to form a molar ratio of 5:1. The solution was stirred for 12 h at 80 °C under Ar-atmosphere. In the glass bottles, 15 mg of CWF, MMCWF, CWF–E, and CWF–EG powders were added separately into 3 mL of the Li2S6 electrolyte to evaluate the Li_2S_6 adsorption ability of samples.

1.3 Characterization

Scanning electron microscope (SEM, ZEISS Sigma 300) and transmission electron microscope (TEM, Jem-2100F) were used to characterize the morphology of the obtained samples. X-ray diffraction (XRD, Dmax2500) and Raman spectroscopy (LabRam HR Evolution) were employed for characterizing the crystalline structure and defect features of the obtained samples. X-ray photoelectron spectroscopy (XPS, Thermo ESCALAB 250XI), Thermogravimetric analysis (TGA, STA6000) was utilized to assess the chemical composition of the obtained samples. The specific

surface area and pore distribution property were analyzed using the BET analyzer (Micromeritics ASAP 2460). The defect structure was investigated using electron paramagnetic resonance (EPR, Bruker EMXplus-6/1). The adsorption capacity of the obtained materials was confirmed through UV–vis spectra obtained using the Lambda-750 UV–vis spectrometer. The tube furnace used was model OTF-1200X-S, provided by Hefei Kejing Material Technology Co., Ltd.

1.4 Electrochemical testing

The working electrodes were formulated by blending the acquired material/S (CWF/S, MMCWF/S, CWF−EG/S and CWF−E/S) (80 wt.%), Super P (10 wt.%), and polyvinylidene difluoride binder (10 wt.%) at N–methyl–2–pyrrolidone. The resulting slurry was uniformly applied to an aluminum foil and dried under vacuum at 55 ℃ for 24 h. The dried electrode was sectioned into 12 mm diameter discs, with the typical areal sulfur mass loading maintained at approximately 1.2 mg cm^{-2}. The thickness of the lithium anode is 0.6 mm, and the diameter is 16 mm. Additionally, a higher areal sulfur loading (2.8 and 5.6 mg cm^{-2}) was deliberately set to assess the performance of the MMCWF/S cathode. A Li wafer was employed as the anode for the LSBs. A polypropylene microporous film, commonly referred to as a Celgard separator, was used as the separator. A solution of 1 M LiTFSI with 1.0 wt% $LiNO_3$ was prepared by dissolving it in a mixture of 1,3-dioxolane (DOL) and 1,2-dimethoxyethane (DME) in a 1:1 (v/v) ratio, serving as the electrolyte. The electrolyte-to-sulfur ratio (E/S) was maintained at approximately 15 $\mu L \cdot mg^{-1}_S$ for standard electrodes and 6 $\mu L \cdot mg^{-1}_S$ for high-loading electrodes, respectively. The cells were assembled within an argon-filled

glovebox, where the water and oxygen content were maintained below 0.01 ppm. Cyclic voltammetry (CV) and electrochemical impedance spectroscopy (EIS) tests were performed using an electrochemical workstation (CHI 660b). EIS measurements were conducted at open circuit potential over a frequency range of 0.01–100 kHz, while CV was executed within a voltage range of 1.7–2.8 V. Galvanostatic charge/discharge curves were obtained using a cell test system (Land CT3002 A) at room temperature and within the voltage range of 1.7–2.8 V.

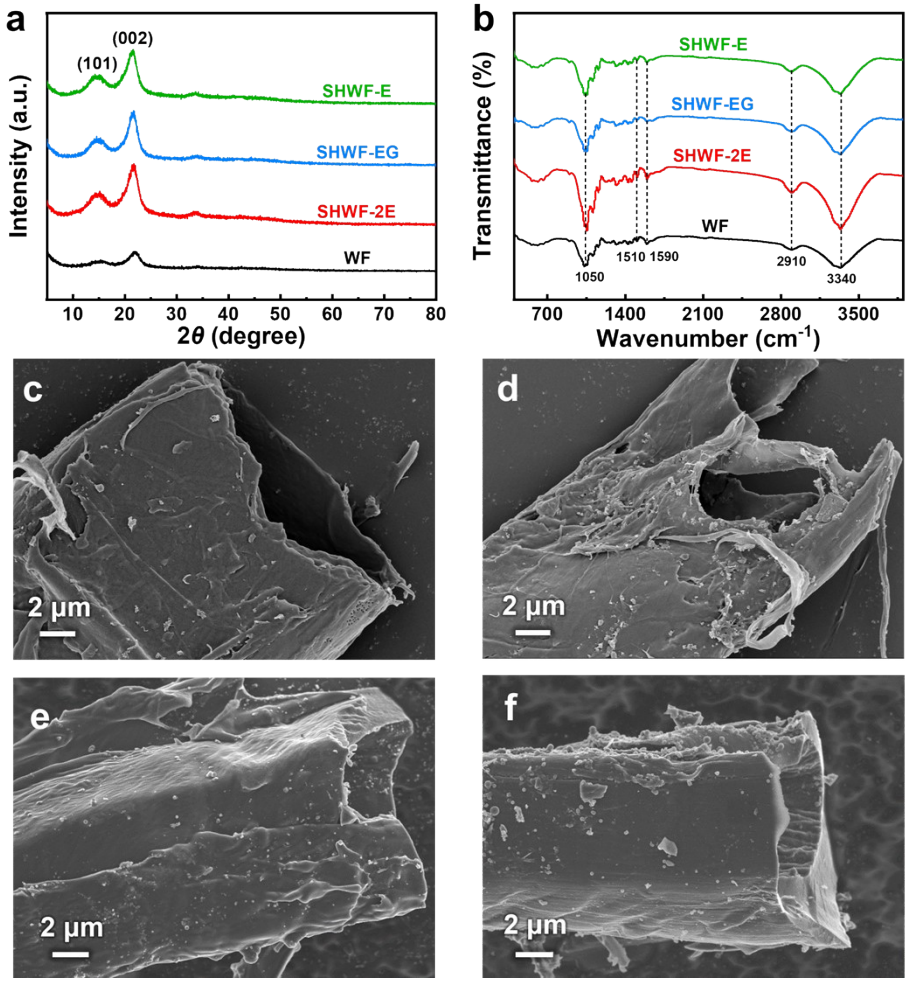

Fig. S1 Morphology and architecture of SHCWF–2E. XRD patterns (a) of the natural WF, SHWF–2E, SHWF–EG, and SHWF–E. FTIR spectra (b) of natural WF, SHWF–2E, SHWF–EG, and SHWF–E. SEM images of natural WF (c) SHWF–2E (d), SHWF–2E (e) and SHWF–EG (f).

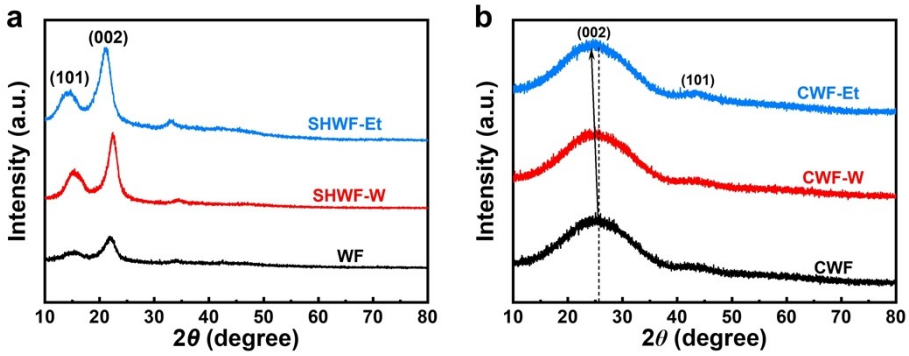

Fig. S2 XRD patterns (a) of the natural WF, SHWF–W, and SHWF–Et. XRD patterns (b) of the natural CWF, CWF–W, and CWF–Et.

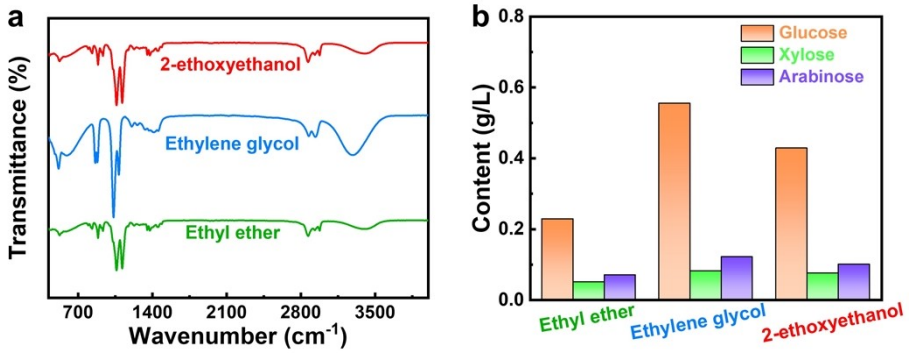

Fig. S3 FTIR spectra (a) and HPLC results (b) of the solutions after solvothermal reactions of wood fibers in ether, ethylene glycol, and ethylene glycol ethyl ether, respectively.

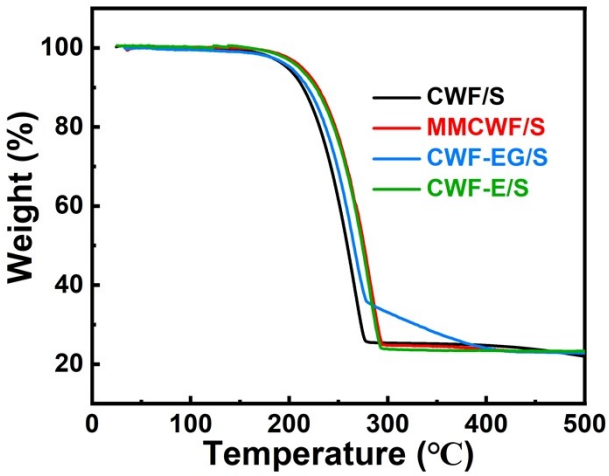

Fig. S4 TGA curves (g) of CWF/S, MMCWF/S, CWF–EG/S and CWF–E/S.

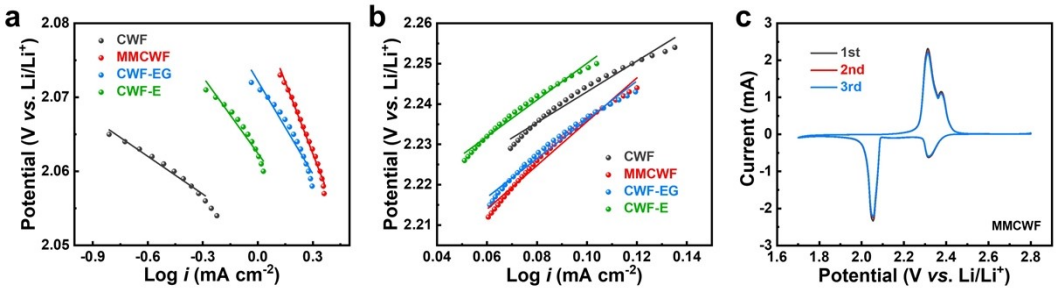

Fig. S5 Tafel plots for the corresponding cathodic reaction (a), and anodic reaction (b) of CWF, MMCWF, CWF–EG and CWF–E. CV curves (c) of MMCWF/S cathode at a scan rate of 0.1 mV s^{-1}.

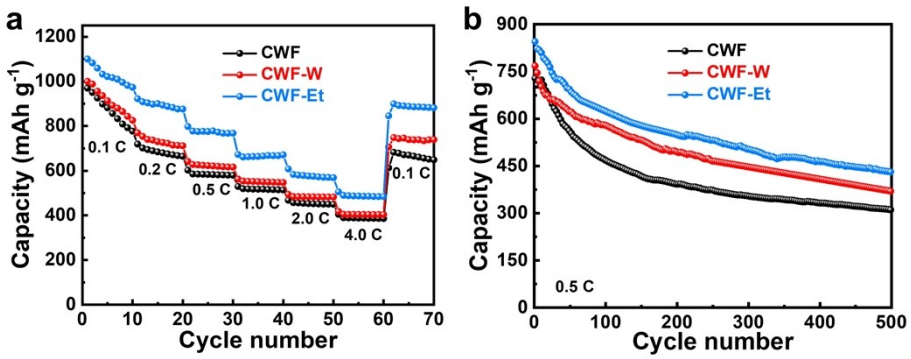

Fig. S6 The rate capability of CWF/S, CWF–W/S, and CWF–Et/S cathode at various current rates from 0.1 to 4.0 C (a). Stability test of CWF/S, CWF–W/S, and CWF–Et/S cathode (b).

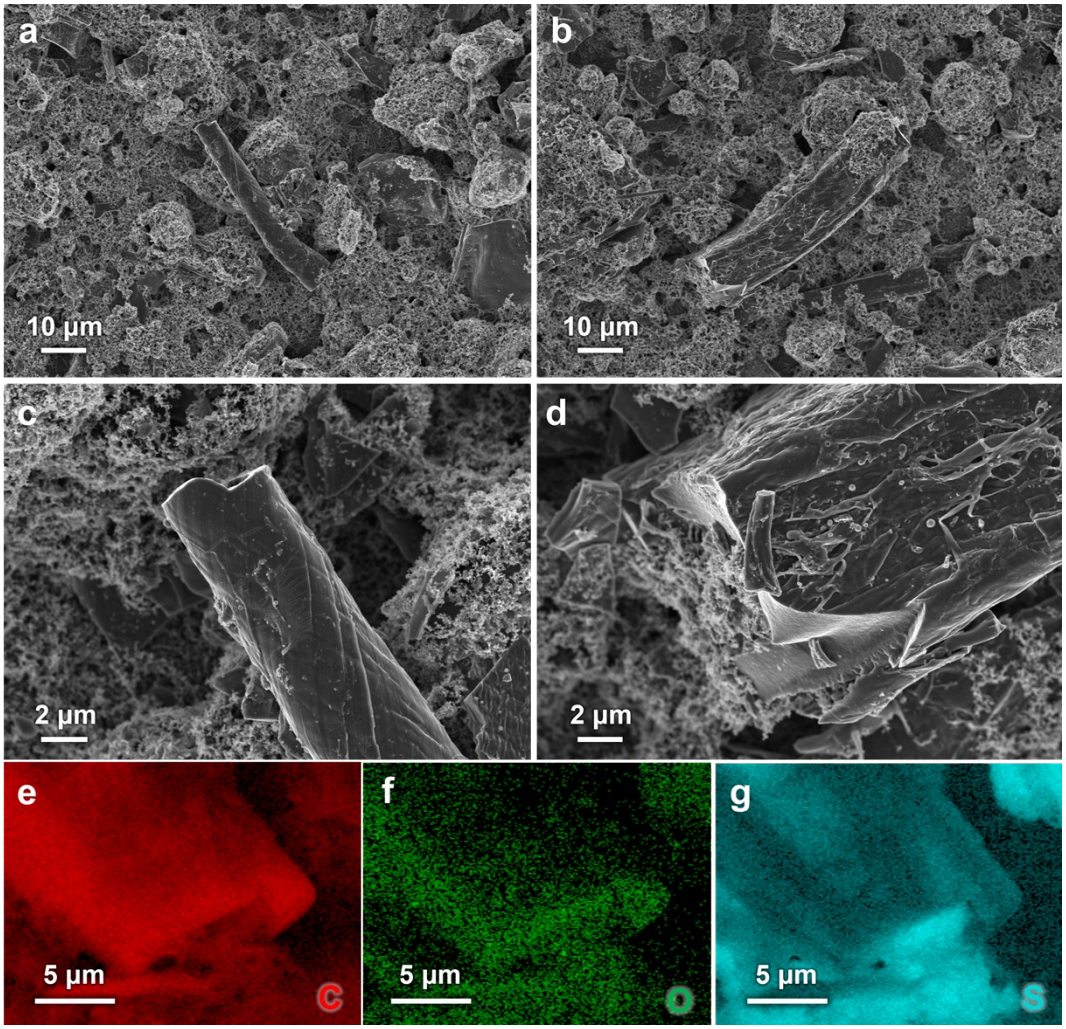

Fig. S7 SEM images of MMCWF before (a, c) and after (b, d) cycling; the corresponding EDX maps of C (e), O (f) and S (g) of the MMCWF after cycling.

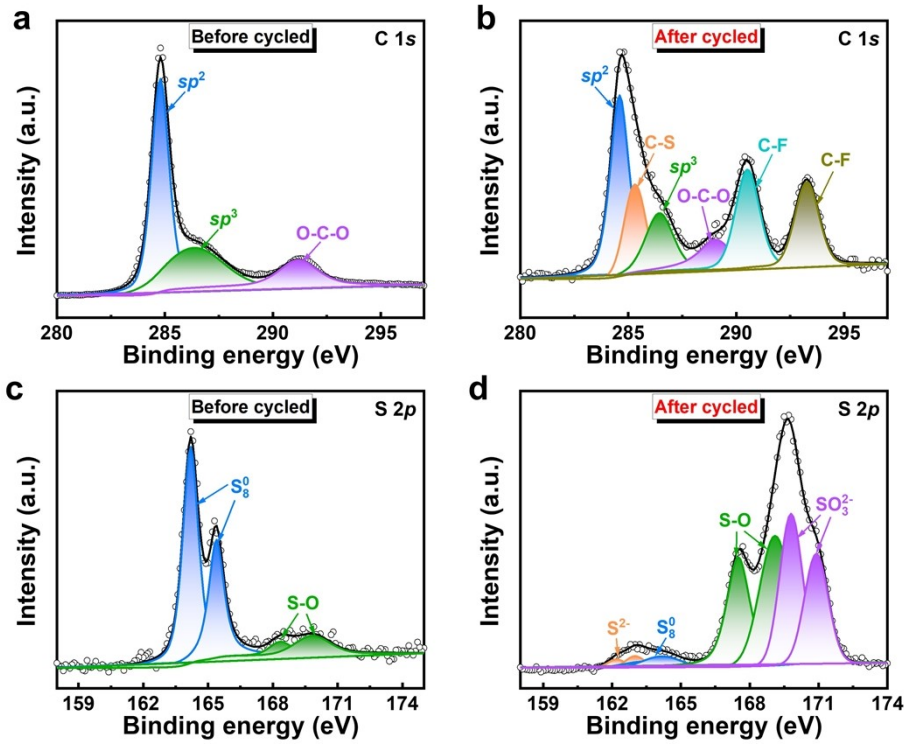

Fig. S8 High-resolution C 1*s* spectrum (a, b) and high-resolution S 2*p* spectrum (c, d) of before and after cycled MMCWF.

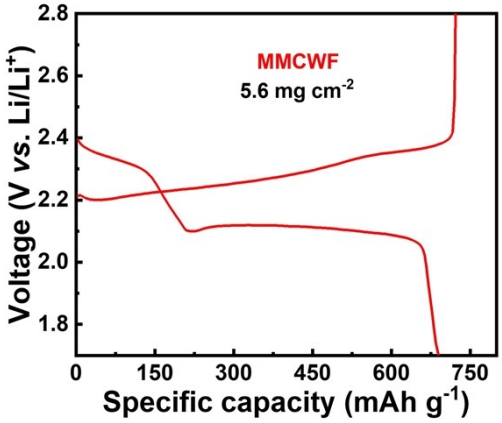

Fig. S9 GDC profile of MMCWF/S under the high S loading.

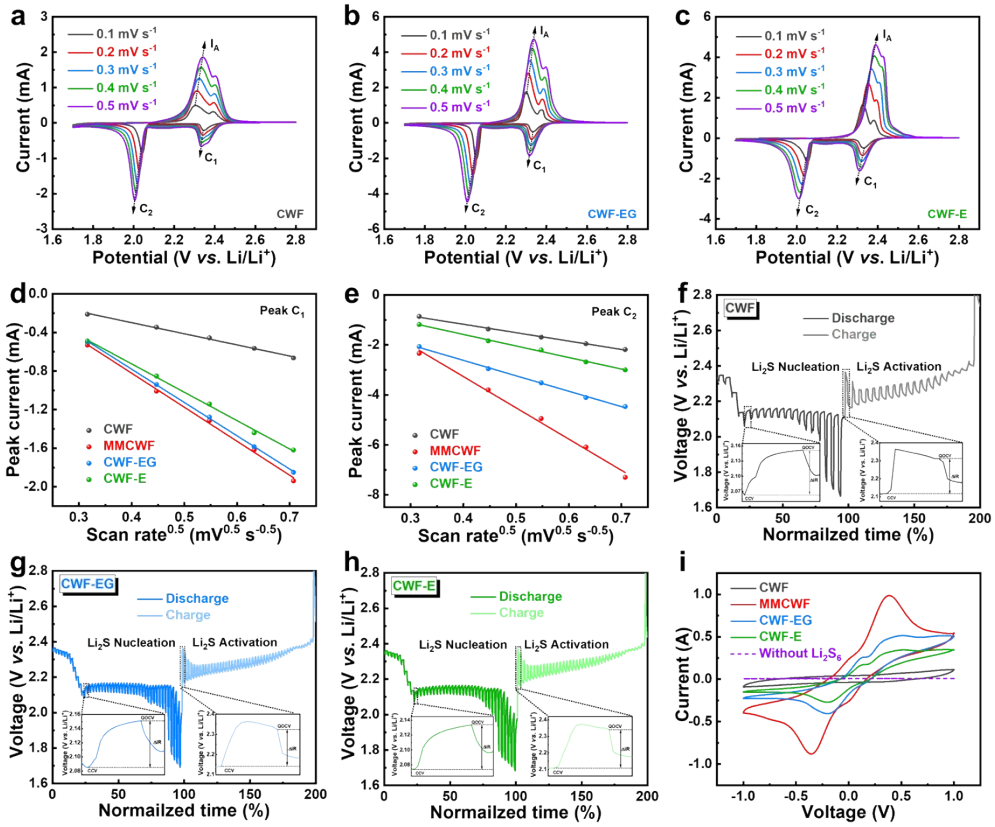

Fig. S10 CV curves of CWF/S (a), CWF−EG/S (b) and CWF−E/S (c) cathodes at different voltage sweep rates. CV peak current values corresponding to processes C_1 (d) and C_2 (e) for CWF/S, MMCWF/S, CWF−EG/S and CWF−E/S electrodes versus square root of scan rates. Galvanostatic intermittent titration (GITT) voltage profiles of CWF (f), CWF−EG (g), and CWF−E (h). CV curves of the symmetric cell at 10 mV s^{-1} (i).

Table S1 The XPS result of CWF, MMCWF, CWF–EG and CWF–E.

Samples	C (*at.* %)	O (*at.* %)
CWF	90.89	9.11
MMCF	92.31	7.69
CWF–EG	93.35	6.65
CWF–E	91.44	8.56

Table S2 Percentages of various C configurations in CWF, MMCWF, CWF–EG and CWF–E.

Samples	C distributions/%		
	sp^2	sp^3	O–C–O
CWF	73.98	14.11	11.91
MMCF	67.22	23.00	9.78
CWF–EG	59.71	24.46	15.83
CWF–E	66.67	18.37	14.96

Table S3 The specific BET result of CWF, MMCWF, CWF–EG and CWF–E.

Samples	Specific surface area (m^2/g)	pore volume (cm^3/g)	Pore size (nm)
CWF	120.5	0.09	4.97
MMCWF	567.5	0.31	2.54
CWF–EG	570.1	0.30	2.22
CWF–E	485.0	0.26	2.71

Table S4 comparison of the specific capacities and current densities between MMCWF and cathodes reported in the literature

Samples	Current density (1 C = 1675 mA h g^{-1})	Cycle number (*n*)	Remaining capacity (mA h g^{-1})	capacity decay per cycle	References
MMCWF	**0.5 C**	**800**	**520.7**	**0.05%**	**This work**
WLC-CNTs	0.2 C	300	547.0	0.12%	[S1]
BPC	0.1 C	100	650.7	0.23%	[S2]
Ni-Co-P@C	0.5 C	1000	414.8	0.056%	[S3]
HPCA-TO	1.0 C	200	513	0.8%	[S4]
Co@N-HCMS	1.0 C	500	540	0.08%	[S5]
TD-HDC	1.0 C	800	466.9	0.12%	[S6]
RSC	0.5 C	300	566.0	0.32%	[S7]
MnS/N-C@CNT	0.5 C	500	500.8	0.17%	[S8]

References

1. N. Wang, X. Zhang, Z. Ju, X. Yu, Y. Wang, Y. Du, Z. Bai, S. Dou, G. Yu, *Nat. Commun.*, 2021, **12**, 4519.
2. Zh. Wang, X. Zhang, X. Liu, Y. Zhang, W. Zhao, Y. Li, C. Qin, Z. Bakenov, *J. Colloid Interf. Sci.*, 2020, **569**: 22-33.
3. Z. Wu, S. Chen, L. Wang, Q. Deng, Z. Zeng, J. Wang, S. Deng, *Energy Storage Mater.*, 2021, **38**, 381–388.
4. C. Shi, J. Huang, Y. Tang, Z. Cen, Z. Wang, S. Liu, R. Fu, *Carbon*, 2023, **202**, 59–65.
5. L. Su, J. Zhang, Y. Chen, W. Yang, J. Wang, Z. Ma, G. Shao, G. Wang, *Nano Energy*, 2021, **85**, 105981.
6. D. Wu, J. Liu, J. Chen, H. Li, R. Cao, W. Zhang, Z. Gao, K. Jiang, *J. Mater. Chem. A*, 2021, **9**, 5497.
7. M. Zhao, Y. Peng, B. Li, X. Zhang, J. Huang, *J. Energy Chem.*, 2021, **56**, 203–208.
8. F. Li, X. Qian, L. Jin, *ACS Sustainable Chem. Eng.*, 2021, **9**, 15469−15477.